Zeitschrift: Helvetica Physica Acta
Band: 65 (1992)
Heft: 1

Vereinsnachrichten: Rapport de la réunion d'automne de la SSP
Autor: [s.n.]

Helv Phys Acta
Vol. 65 (1992)

0018-0238/92/010109-22$1.50+0.20/0

High-resolution photoemission in the quasi-unidimensional $K_{0.3}MoO_3$ compound.

B. Dardel, D. Malterre, M. Grioni, P. Weibel, Y. Baer and C. Schlenker*

Institut de Physique, Université de Neuchâtel, CH 2000 Neuchâtel Switzerland
* L.E.P.E.S. CNRS B.P. 166, 38042 CNRS Grenoble Cedex, France

abstract : High resolution photoemission measurements have been carried out on the blue bronze ($K_{0.3}MoO_3$). In this system, a metal-insulator transition occurs at 180 K associated with a lattice distortion and formation of charge density waves (CDW). From photoemission experiments on the valence band, we estimate the Peierls gap and its evolution with temperature. An anomalous behaviour of the spectral function at the Fermi level is observed and is discussed in terms of marginal Fermi liquids.

The quasi-unidimensional blue bronze undergoes a Peierls transition at T=180 K to a charge density wave insulating state [1]. This structural and electronic transition leads to a energy gap opening in the density of states which has been estimated between 100-150 meV from resistivity and optical measurements. The aim of this study is to directly measure this gap from UV high-resolution photoemission experiments (energy resolution better than 20 meV).

Figure 1 shows the spectral function of the blue bronze for two temperatures, above and below the Peierls temperature. A transfer of the spectral weight to higher binding energy is clearly shown in the T=40 K spectrum. This behaviour reflects the opening of an energy gap which can be estimated to 2Δ=100meV from the shift of intensity at the Fermi level (E_F). In

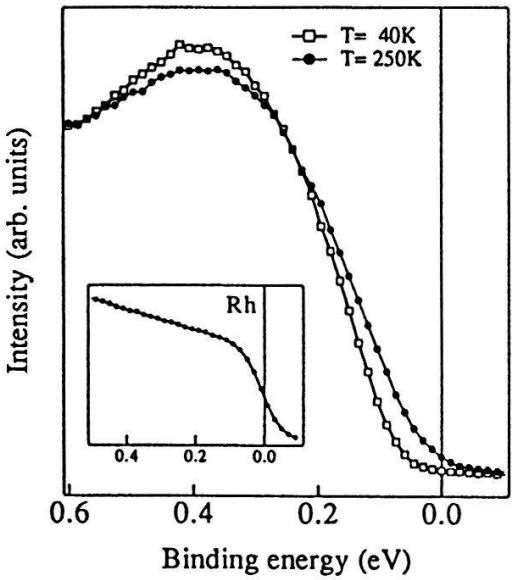

Figure 1 : spectral function of $K_{0.3}MoO_3$ for T= 40 K and T=250 K. In the insert we report the experimental spectrum of Rh metal at 300 K.

figure 2, this "spectroscopic" gap is reported as a function of temperature. The transition is clearly shown near 180 K but the gap does not follow a BCS dependence as expected in the Fröhlich model. On the other hand, the T=250 K spectrum does not exhibit the typical metallic signature. A metal is characterized by an incompletely filled density of states (DOS) that leads to a discontinuity at E_F in the spectral function as shown on the Rh spectrum in the insert of figure 1. Moreover in the Fröhlich model, a gap opening is accompanied by a peak in the spectrum at $E=E_F-\Delta$ which is not experimentally observed. Such behaviours strongly suggest that the spectral function differs from the DOS due to many body effects (electron-phonon and electron-electron interactions). Several mechanisms could be invoked to explain these observations. Fluctuations are very important in one-dimensional system and result in a lowering of the spectral intensity near E_F [2]. On the other hand, one-dimension correlations are very singular: 1-d metals are no longer Fermi liquids and their excitations cannot be described in terms of quasi-particles. As a consequence, the photoemission spectral function exhibits a vanishing intensity at E_F as demonstrated in the exactly solvable Luttinger model [3].

To summarize, photoemission measurements clearly show that the spectral function reflects the transition from metallic to CDW state. Nevertheless, the photoemission spectra cannot be described in a simple model neither for the metallic nor for the semiconductor state. This result suggests that unusual mechanisms associated to the dimensionality of the system strongly affect the spectral function.

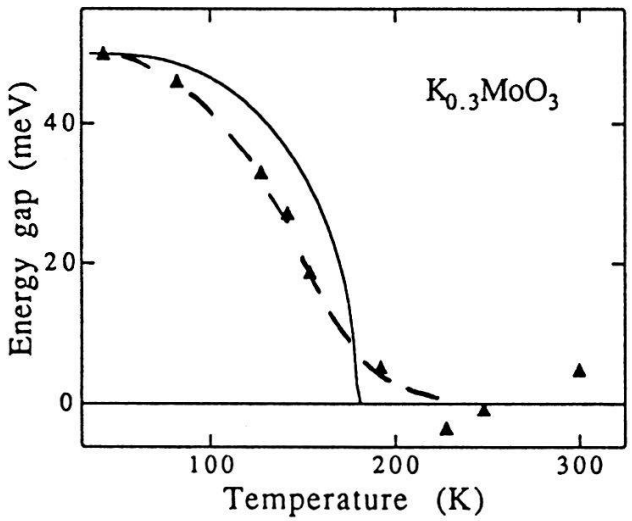

Figure 2 : Temperature dependence of the energy gap deduced from photo -emission measurements. The dashed line is a guide for the eye, and the solid line is a BCS curve.

References

[1] C. Schlenker et al, Low-dimensional electronic properties of molybdenum bronzes and oxides, Ed. C. Schlenker, Kluwer Academic Publisher, 159 (1989).
[2] M.J. Rice and S. Strässler, Solid State Commun. 13, 1389 (1973).
[3] H.J. Schulz, Int. J. Mod. phys. B 5, 57 (1991).

Xenon Dendrites

E. Hürlimann, U. Bisang and J.H. Bilgram
Laboratorium für Festkörperphysik, ETH, 8093-Zürich

Experiments have been performed to study the shape of free growing xenon dendrites into the pure, supercooled melt. A new set of parameters is proposed to characterize the shape of a dendrite with many interacting sidebranches: The length of the contour U and the area of projection F of the dendrite. We find a linear relationship between F and U. The normalized slope (dF/dU)/R, where R is the radius of curvature of the dendrite tip, is independent of the supercooling ΔT. This means that the ratio of volume to surface of a dendrite is proportional to R.

The experimental setup is similar to the one described in [1]. The measurements have been performed for supercoolings 25 mK < ΔT < 150 mK. Fig. 1 shows several contours of a xenon dendrite grown at a supercooling of about 98 mK. The contours have been extracted from video-pictures taken at 90s intervals. Three stages can be distinguished in dendritic solidification: The steady-state growth of the parabolic tip, the nearly regular evolution of the first sidebranches some tip radii behind the tip and the coarsening of the structure due to the competition of sidebranches. In previous studies various parameters have been used to characterize the dendrite, e.g. the radius of curvature of the tip R, the sidebranch spacing S, the amplitude of the sidebranches w. These parameters do not describe the nonlinearity of the dendritic growth like the interaction between the side-

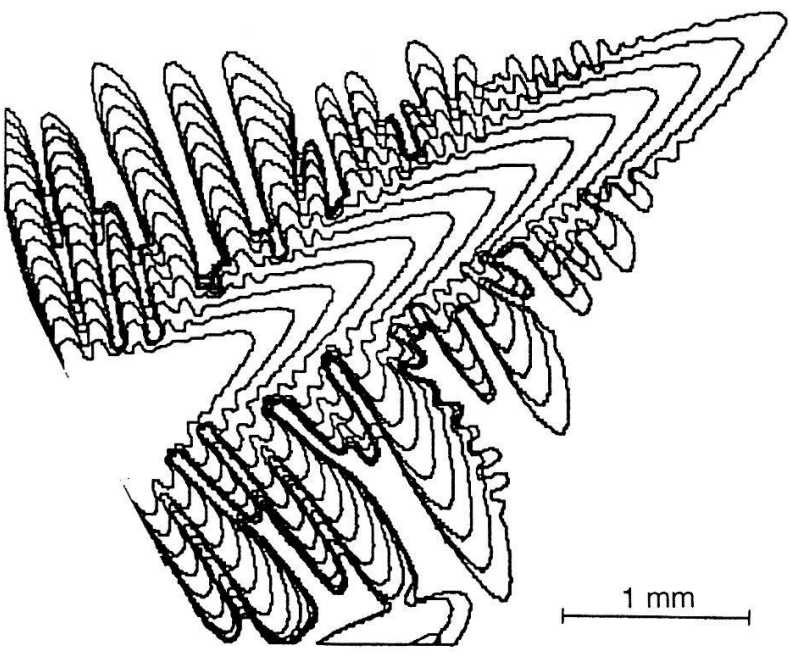

Fig. 1 Contours of a xenon dendrite at 90 s intervals.

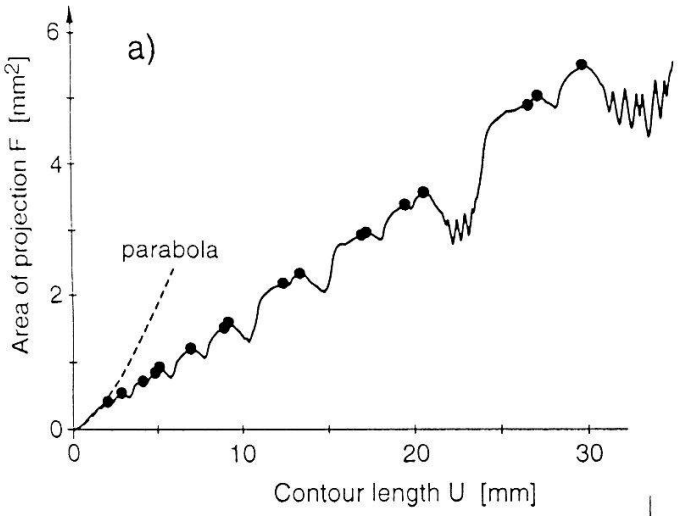

Fig. 2a Area of projection F vs the contour length U of a xenon dendrite.

Fig. 2b Contour of one side of a xenon dendrite.

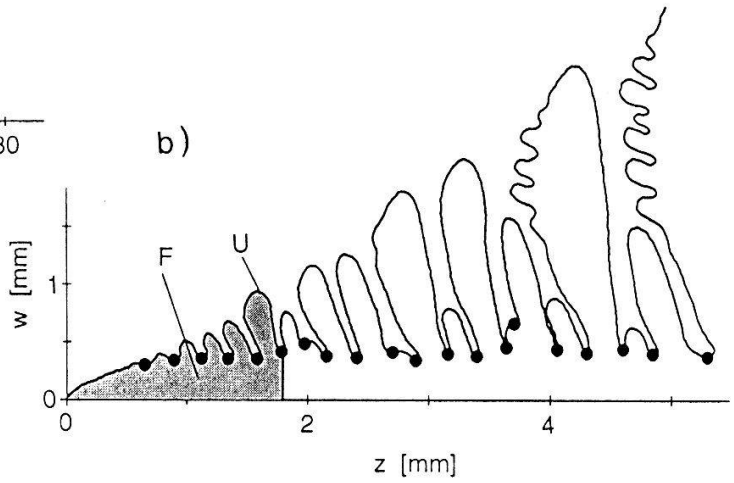

branches. We choose the contour length U and the area of projection F of the dendrites (Fig. 2b) as new parameters to study the overall behavior of the dendrites. Fig. 2a. shows F as a function of U measured for the dendrite depicted in Fig. 2b). The dashed line represents a parabola fitted to the dendrite tip. Behind the tip region F increases linearly with U. To determine the slope (dF/dU), a line is fitted to the points designated by dots in Fig. 2a). The normalized slope (dF/dU)/R is plotted vs. the dimensionless supercooling Δ in Fig. 3. It is independent of the supercooling.

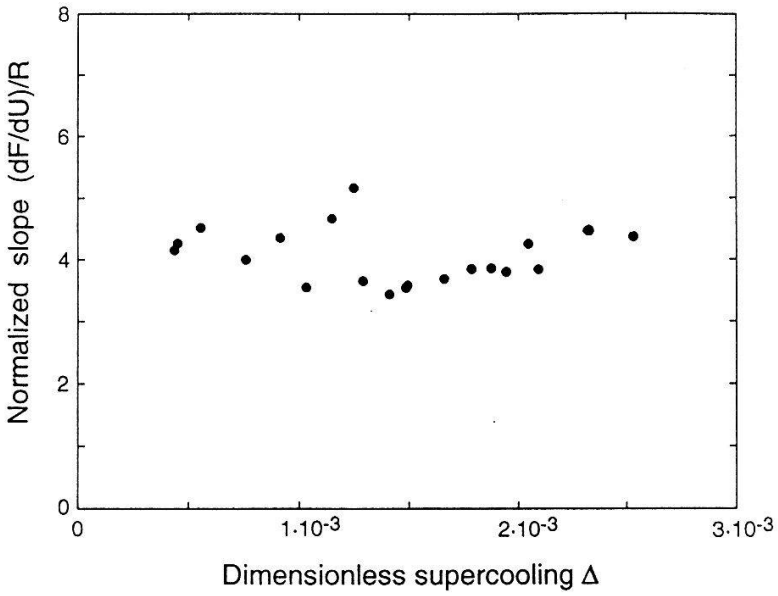

Fig. 3 The normalized slope (dF/dU)/R vs the dimensionless supercooling Δ.

Acknowledgements: We thank Prof. H.R. Ott for his support. This work is supported by the Swiss National Science Foundation.

[1] J.H. Bilgram, M. Firmann and E. Hürlimann, J. Crystal Growth, 96, 175 (1989)
E. Hürlimann, V. Peschak and J.H. Bilgram, Helv. Phys. Acta, 64, 185 (1991)

Surface stucture of ultrathin, epitaxial $CoSi_2$ films on Si(100) observed by scanning tunneling microscopy

H. Sirringhaus, R. Stalder, C. Schwarz, H. von Känel
Laboratorium für Festkörperphysik, ETH Zürich, 8093 Zürich

Abstract
We report on the first scanning tunneling microscopy (STM) study of epitaxial $CoSi_2$ grown on Si(100) by molecular beam epitaxy (MBE). By applying a suitable template technique, epitaxial $CoSi_2$ films of pure (100) orientation with thicknesses between 10–100Å were grown and investigated by in–situ STM. On the basis of atomic–scale resolution STM topographs the structural properties of the different reconstructions observed on Co– and Si– rich surfaces are discussed.

In Si technology there is an increasing demand for epitaxial metallic contacts on Si(100) surfaces. The growth of $CoSi_2$ overlayers on Si(111) is now well under control, while it is complicated on Si(100) due to the coexistence of several different epitaxial orientations. These generally lead to a multi–grain film structure. Recently, this problem has been solved by the use of either a Co implantation [1] or a MBE template techniqe [2]. In our studies we applied the latter method to grow single–crystalline, epitaxial silicide films with pure (100)–orientation ($CoSi_2$[100]|| Si[100], $CoSi_2$[011]|| Si[011]) on Si(100) substrates with thicknesses between 10–100Å. The sample preparation technique is similar to the one used on Si(111) and has been described elsewhere [2,3].
In the following we will summarize our STM results on the various surface reconstructions.
Fig.1 shows the $(\sqrt{2}x\sqrt{2})R45$ reconstruction characteristic of Co–rich surfaces (which could, for example, be prepared by capping the silicide with 1Å of Co and annealing at 450° C): on top of the quadratic protrusions a weak fourfold corrugation of 0.03–0.04Å with a distance of 3.0–3.2Å between opposite maxima (indicated by the black dots) has been detected. The holes at the corners of each square have a maximum depth of ~0.4Å.
Si–rich surfaces exhibited a more complex structure. The most characteristic reconstruction is of $(3\sqrt{2}x\sqrt{2})R45$ type (Fig.2): its dominant feature is the shift of atomic corrugation maxima from position "a" to "b" in two neighbouring [001]–chains, while in every third chain they remain in position "a". The $(3\sqrt{2}x\sqrt{2})R45$ regions are surrounded by a $(\sqrt{2}x\sqrt{2})R45$ reconstruction, which is clearly distinct from the one found on Co–rich surfaces. It could not be identified in a previous low energy electron diffraction (LEED)

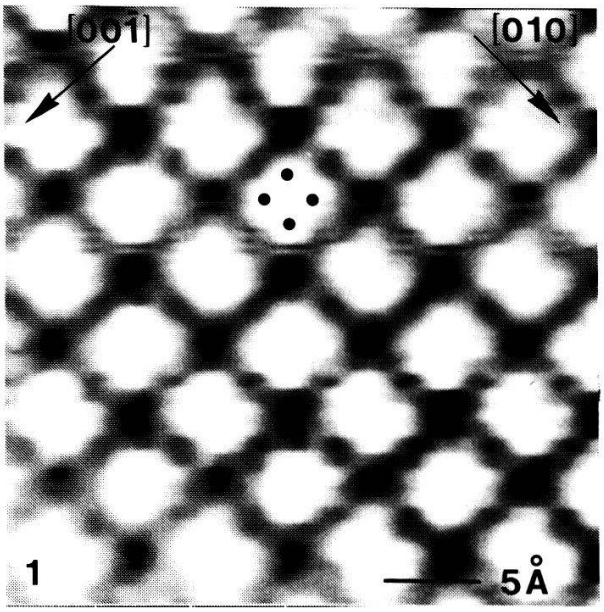

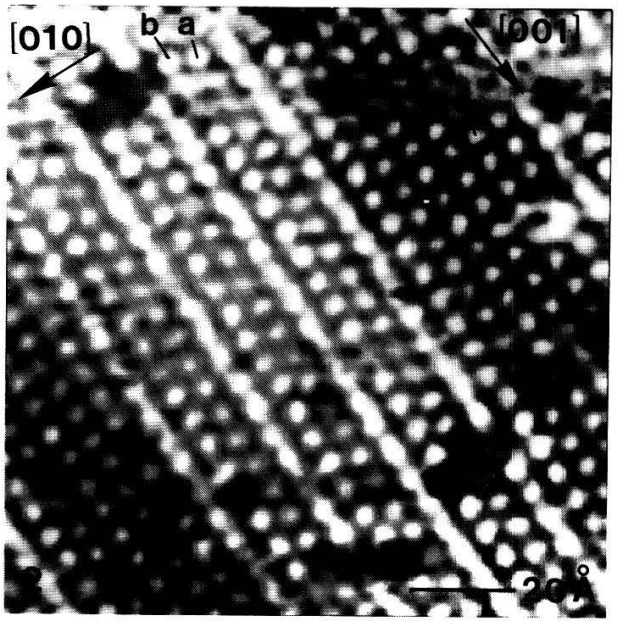

Fig 1: $(\sqrt{2}x\sqrt{2})R45$ on a Co–rich surface (V_{sample}= –5mV, I_t= 40nA)
Fig.2: $(3\sqrt{2}x\sqrt{2})R45/(\sqrt{2}x\sqrt{2})R45$ on a Si–rich surface (V_{sample}= –10mV, I_t= 4nA)

study [2]. Corrugation maxima are in position "a" with typical corrugation amplitudes up to 1.2Å.

Predominantly Co–rich surfaces often exhibited 1.36Å high islands with a $(3\sqrt{2}x\sqrt{2})R45/(\sqrt{2}x\sqrt{2})R45$ reconstruction on top. This suggests that the Si–rich surface has one additional plane of Si with respect to the Co–rich surface.

When heating the template a mixed $(\sqrt{2}x\sqrt{2})R45$/2x2 reflection high energy electron diffraction (RHEED) pattern usually appeared at temperatures between 150–200° C. The 2x2 seems to be a metastable phase on Si–rich parts of the surface, which evolves into the stable $(3\sqrt{2}x\sqrt{2})R45$ at higher temperatures. We have developed a structure model for the various reconstructions, which will be described in detail in a future publication. Starting from the unreconstructed, Si–terminated silicide surface, the quadratic protrusions on the Co–rich surface can be well accounted for by a lateral movement of four neighbouring Si atoms towards each other to form a bonding configuration. In our model the Si–rich surface consists of half a monolayer of additional Si bound on top of the Co–rich surface.

[1] A.E. White, K.T. Short, R.C. Dynes, J.P. Garno, J.M. Gibson, Appl. Phys. Lett. 50, 95 (1987)
[2] S.M. Yalisove, R.T. Tung, J.L. Batstone, Mat. Res. Soc. Symp. Proc. 116, 439 (1988)
[3] R. Stalder, H. Sirringhaus, N. Onda, H. von Känel, Surf. Sci. (in press)

Critical Current and Activation Energy Due to Two Dimensional Layered Structure in $Bi_2Sr_2CaCu_2O_{8+y}$ Film

T. Fukami*, T. Yamamoto**, Y. Yamasaki**, K. Miyoshi**, V. Soares, Y. Horie**, F. Ichikawa**, H. Nakano***, T. Aomine** and L. Rinderer

Institut de Physique Expérimentale, Université de Lausanne, CH-1015 Lausanne, Switzerland
* On leave from Department of Physics, Kyushu University, Fukuoka 812, Japan
** Department of Physics, Kyushu University, Fukuoka 812, Japan
***Department of Physics, College of General Education, Nagoya University, Nagoya464-01, Japan

Abstract: Temperature T dependence of critical current density $J_c(T,H)$ was measured for $Bi_2Sr_2CaCu_2O_{8+y}$ films in magnetic fields $\boldsymbol{H}$ // the basal plane. Plots of $J_c(T,H)$ vs. $(1-t)$, $(t = T/T_c)$, revealed a power n dependence near T_c $(1.5 \geq n \geq 1.35)$ and a linear dependence at intermediate temperatures, and tended to saturate with decreasing temperature. This behavior is compared with that one expected from the intrinsic pinning model.

The intrinsic pinning model based on the short coherence lengths and two dimensional layered crystal structure proposed in [1,2] could explain the different temperature T dependence of the activation energy $U(T,H)$ for different oxide superconductors in magnetic field $\boldsymbol{H}$ // the basal plane [3]. In the present work we discuss the behavior of the critical current density $J_c(T,H)$ vs. T for $Bi_2Sr_2CaCu_2O_{8+y}$ (BSCC) films in $\boldsymbol{H}$ // the basal plane and we compare the obtained results with those one expected from the model.

Thin films of BSCC were prepared by laser ablation technique by depositing on single crystalline MgO(100) substrates at room temperature. As-deposited films were processed thermally. The c-axes of crystallites oriented perpendicularly to the surface of the substrate.

Figure 1 shows the plots of $J_c(T,H)$ vs. $(1-t)$ for $\boldsymbol{H}$ // the basal plane. Here $t = T/T_c$ with the critical temperature T_c defined as a peak position of dR/dT vs. T curve in $H=0$, where R is the electrical resistance. $J_c(T,H)$ shows $(1-t)^n$ dependence near T_c and a linear one of $(1-t)$, and tends to saturate with decreasing temperature, where $n=1.35$ for $H=0.049$ kG, $n=1.4$ for $H = 1.25$ kG and $n=1.5$ for $H=4.74$ kG.

Since $J_c(T,H)$ vs. the angle between $\boldsymbol{H}$ and the basal plane could be explained qualitatively by the intrinsic pinning model [4], here the temperature dependence of $J_c(T,H)$ is calculated by using a theoretical formula predicted by the same model for the critical current density,

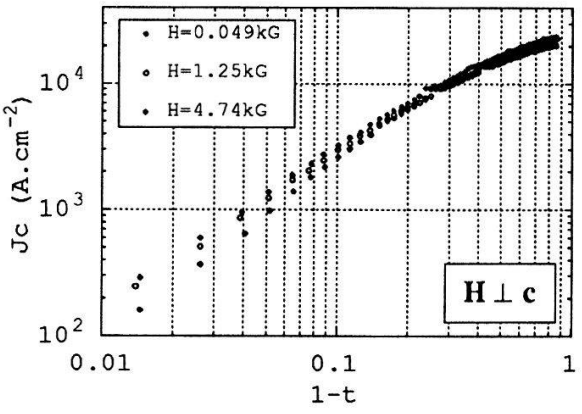

Fig. 1 Temperature dependence of the critical current density for $\boldsymbol{H}$ // the basal plane.

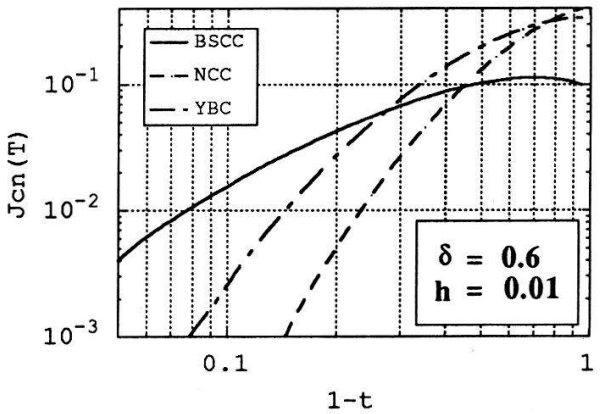

Fig. 2 $J_{cn}(T,H)$ in eq. (2) vs. $(1-t)$ for BSCC, NCC and YBC. Here $h=H/H_{c2}(0)$.

$$J_c(T,H)=c[H_c^2(0)/(8\pi B_0 a_c)](\xi_{ab}/\xi_c)\eta_M(1-t^2)^2[1 - H/H_{c2}(T)]$$
$$\equiv c[H_c^2(0)/(8\pi B_0 a_c)](\xi_{ab}/\xi_c)J_{cn}(T,H), \quad (1)$$

to explain the experimental results. Here c is the light velocity; $H_c(0)$ is the thermodynamic critical field at T=0 K; B_0 is defined by $\phi_0/2\pi a_c^2$ with the magnetic flux quantum $\phi_0=hc/2e$ and an inter-distance a_c between successive CuO_2 planes; ξ_{ab} and ξ_c are coherence lengths parallel and perpendicular to the basal plane, respectively; η_M is the maximum value of $\eta(z_0)$ given by eq. (6) in [1] with respect to the position z_0 of a magnetic flux line along the c-axis; $H_{c2}(T)$ is the upper critical field. Since BSCC and $YBa_2Cu_3O_7$ (YBC) have two and one pairs of CuO_2 planes in a crystallographic unit cell, respectively, the original formula was changed a little and it is assumed that one pair of CuO_2 planes is located at z=0 and $z=z_1$ along the c-axis. Figure 2 shows $J_{cn}(T,H)$ in eq. (1) vs. $(1-t)$ for three cases; (i) BSCC with $\xi_{ab}(0)$=15 Å, $\xi_c(0)$=1.0 Å, $a_c=c/2$=15.4 Å with the lattice constant c and z_1= 3.38 Å; (ii) $(Nd_{1-x}Ce_x)_2CuO_4$ (NCC) with $\xi_{ab}(0)$=70 Å, $\xi_c(0)$=2.3 Å and $a_c=c/2$=6.05 Å; (iii) YBC with $\xi_{ab}(0)$=15 Å, $\xi_c(0)$=2.5 Å, $a_c=c$=11.7 Å and z_1= 3.25 Å. A parameter δ in Fig. 2 is a measure of spatial variation of the superconducting order parameter [1]. $J_{cn}(T,H)$ vs. $(1-t)$ for BSCC is similar to the experimental results except an extremum at low temperatures. This extremum has not been observed in BSCC films, but its disappearance may be explained as it is discussed below.

When $J_c(T,H)$ is determined by the electrical transport in the mixed state, the threshold voltage used for determination of $J_c(T,H)$ contains the voltage due to flux creep. Therefore, to compare $J_c(T,H)$ vs. $(1-t)$ with $J_{cn}(T,H)$ vs. $(1-t)$, the effect of flux creep must be taken into consideration as discussed in [5]. For the intrinsic pinning model, those ones used in [5] must be replaced by some new constant factors by considering their physical meaning. But we can use the formula,

$$J_c(T,H) \propto J_{c0}(T,H)[\ 1 + (k_BT/U(T,H))\ \ln\ (E_c/a_cB\Omega_0)\ ], \quad (2)$$

as long as the temperature dependence is considered. Here $J_{c0}(T,H)$ is the critical current density in the absence of flux creep, E_c is a threshold voltage used for determining $J_c(T,H)$ experimentally, B is the magnetic flux density and Ω_0 is some characteristic frequency of the flux line vibration. Within reasonable parameters, the second term in eq. (2) works as a minus correction term which is larger at high temperatures than at low ones. Therefore, if $J_{cn}(T,H)$ is proportional to $J_{c0}(T,H)$, the degree of the extremum in $J_{cn}(T,H)$ vs. $(1-t)$ is weaken and the theoretical temperature dependence would approach to the experimental results. Furthermore, in order to obtain another confirmative evidence, it would be necessary to observe the temperature dependence of $J_c(T,H)$ for NCC much stronger than for BSCC.

The authors in University of Lausanne are indebted to the Swiss National Science Foundation for financial support. A part of this work was supported financially by a Grant-in Aid for Scientific Research on Priority Areas "Mechanism of Superconductivity" from the Ministry of Education, Science and Culture of Japan.

References

[1] M. Tachiki and S. Takahashi, Solid State Commun. **70**, 291 (1989).
[2] M. Tachiki and S. Takahashi, Solid State Commun. **72**, 1083 (1989).
[3] T. Fukami, K. Hayashi, T. Nishizaki, Y. Horie, V. Soares, T. Aomine and L. Rinderer, Proc. Intern. Conf. on Advanced Materials (May 1991, Strasbourg).
[4] T. Fukami, T. Yamamoto, T. Nishizaki, Y. Horie, F. Ichikawa, V. Soares, T. Aomine and L. Rinderer, Proc. Intern. Conf. on Physics in Two Dimensions (August 1991, Neuchâtel).
[5] D. Dew-Hughes, Cryogenics **28**, 674 (1988).

Preparation of $(Bi_{1-x}Pb_x)_2Sr_2Ca_2Cu_3O_{10}$ Films by RF-Sputtering with Compound Powder Target of Stoichiometric Composition

T. Fukami*, E. Holguin, H. Nakano**, K. Schenk and L. Rinderer

Institut de Physique Expérimentale, Université de Lausanne,
CH-1015 Lausanne, Suisse
* On leave from Department of Physics, Kyushu University, Fukuoka, Japan
**Department of Physics, College of General Education, Nagoya University, Nagoya, Japan

Abstract: Using mixed raw powders with the composition of $(Bi_{1-x}Pb_x)_2Sr_2Ca_2Cu_3O_y$ as a target, roles of Pb content and post-thermal processing conditions were investigated. X-ray powder analysis was performed to characterize films.

1. Introduction

Bulk samples of single phase $(Bi_{1-x}Pb_x)_2Sr_2Ca_2Cu_3O_{10}$ (H-BSCC) can be prepared without a great difficulty by processing thermally for a long time, but it is not so easy to obtain films in single phase of H-BSCC. Using mixed raw powders Hayakawa et al. prepared almost single phase of H-BSCC [1] with non-stoichiometric compound powder target. On the other hand using the stoichiometric composition of Bi_2Pb_x $Sr_2Ca_2Cu_3O_y$ as a target, rather high quality films were prepared [2,3], but under these conditions reproducibility was not so good. In order to improve the reproducibility of preparation and examine the process of the growth of H-BSCC, here the roles of Pb content and post-thermal processing conditions are examined.

2. As-deposited Film Preparation

Targets used here were prepared by mixing raw powders of Bi_2O_3, $SrCO_3$, $CaCO_3$, CuO and PbO by a ratio of Bi:Pb:Sr:Ca:Cu=2:x:2:2:3, dissolving the mixture in ethyl alcohol and drying out the solvent. Thin films of H-BSCC were prepared by RF magnetron sputtering and deposited on MgO (100) substrates kept at 600 °C. Sputtering conditions were as follows: Ar pressure 0.1 mTorr; RF power 100 W; the diameter of powder target 80 mm; the deposition time 2 hours.

3. Experimental Results and Discussion

As-deposited films were treated thermally in a closed furnace with a volume of 33×15×20 cm^3 together with a bulk sample which was prepared by sintering powder with a composition of $(Bi_{0.8}Pb_{0.2})_2Sr_2Ca_3Cu_4O_y$ for about 140 hours. The temperature was increased by 10 hours and kept at the process-temperature T_p for a process time t and then decreased by about 8 hours.

To characterize the films, two X-ray diffraction peaks with common Miller indices (002) due to H-BSCC (at Brag angle 2θ =4.8°) and $Bi_2Sr_2CaCu_2O_8$ or L-BSCC (at 2θ=5.8 °) were observed. To eliminate the effect of preferred orientation of grains in the film as much as possible, the film was rotated around the axis perpendicular to the substrate surface. The electrical resistance $R(T)$ as a function of the temperature T was also measured. For samples containing more than about 40 % H-BSCC, the characteristics were almost the same due to the percolation among the H-BSCC grains though the value of $dR(T)/dT$ was different. Therefore, here we show only X-ray data to estimate the dependences of the ratio of H-BSCC to L-BSCC on the temperature and time.

3.1. Role of Pb

We have tried to prepare films using targets with Pb composition of x = 0.5, 0.7, 0.8, 0.9 and 1.0. The best result was obtained in the range of x comprised between 0.7 and 0.9. As described below, films containing about 60 % of H-

BSCC can be prepared reproducibly for x=0.8 using the best condition of heat treatments known at present.

3-2. Temperature dependence

Figure 1 shows the T_p-dependence of the (002)-line intensity for films prepared using a powder target with x=0.8. All films were processed during a time t =10 hours. The process-temperature sensitively affects the growth of H-BSCC. The maximum ratio with respect to L-BSCC was obtained at 861±1 °C.

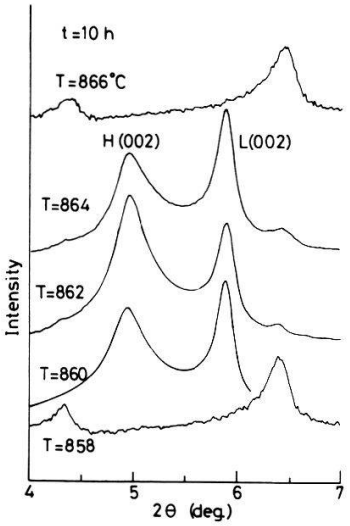

Fig. 1 Process-temperature dependence.

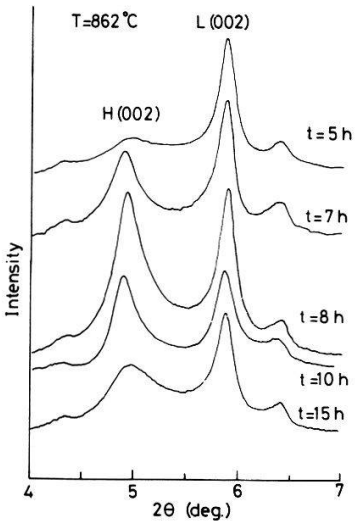

Fig. 2 Process -time dependence.

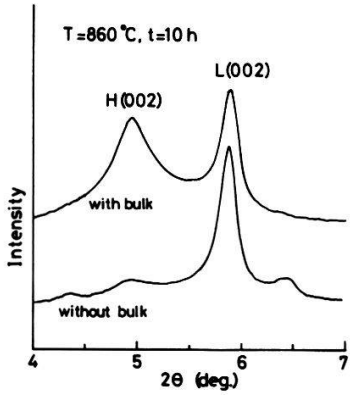

Fig. 3 Role of a bulk sample.

3-3. Process-time dependence

Figure 2 shows the t-dependence of the (002)-line intensity for films prepared at T_p = 862 °C using a powder target with x=0.8. The H-BSCC phase begins to grow after 5 hours and reaches the maximum ratio around 10 hours. However, beyond 15 hours, the peak intensity of the (002)-line corresponding to H-BSCC tends to decrease.

3-4. Role of the bulk sample

Figure 3 shows the data for films processed with and without a bulk sample, respectively, under the conditions of T_p = 860 °C and t= 10 hours. The bulk sample near the film strongly affects the formation of H-BSCC phase. But at present it is not clear what element gives the prominent effect. To inclose the film and the bulk sample in narrower space made the effect more prominent.

4. Summary

Bi-Sr-Ca-Cu-O films were prepared by RF-sputtering technique using as a target a non-sintered compound powder of stoichiometric composition with x=0.8. After treating thermally the as-deposited films in a closed chamber with a H-BSCC bulk sample under the condition of T_p=861 ± 1 °C and t = 10 hours, a ratio of 60 % could be obtained reproducibly for the H-BSCC phase.

Acknowledgments

The authors are indebted to the Swiss National Science Foundation for financial support. The authors wish to thank Mr. F. Bommeli for helping us to prepare films and taking X-ray data.

References

[1] H. Hayakawa, M. Kaise, K. Nakamura and K. Ogawa, Jpn. J. Appl. Phys. 28, L967 (1989).

[2] S. Nicoud, H. Nakano, D. Abukay, M. Suzuki, B. Dutoit and L. Rinderer, Helv. Phys. Acta 64, 179 (1991).

On the rôle of fluctuations for reaction-diffusion phenomena.

Bastien Chopard[1], Stephen Cornell[2] and Michel Droz[2]

(1) Groupe de calcul parallèle, SEINF Université de Genève, CH-1211 Genève 4.
(2) Département de Physique Théorique, Université de Genève, CH-1211 Genève 4.

We review the importance of fluctuations in both homogeneous and inhomogeneous reaction-diffusion phenomena for the general two-species reaction $nA + mB \rightarrow$ inert. Heuristic arguments suggest that the temporal decay of the particle densities differs from the prediction of the rate equations in dimensionality less than some critical value d_{up}. In the homogeneous case these arguments yield $d_{up} = 4$ and 2 for random and correlated initial conditions respectively, whereas a value $d_{up} = 2$ is predicted for inhomogeneous situations where A and B are initially segregated and react within a confined front. These results are compared with numerical cellular automata simulations.

Chemical reactions in which several species react are usually described in terms of macroscopic rate equations which give the time evolution for the local average concentrations of the different species. These assume that the reaction is completely described by the local average densities, i.e. the reaction introduces no correlations between the reacting species. This mean-field approximation neglects an important aspect of the problem, namely the microscopic fluctuations. One of the simplest example is provided by the irreversible reaction in which particles of the species A and B diffuse in a medium and react to form an inert species: $A + B \rightarrow$ inert. The rate equations are:

$$\partial_t a = D\nabla^2 a - k_1 R, \qquad \partial_t b = D\nabla^2 b - k_2 R, \tag{1}$$

where $a(\vec{r},t), b(\vec{r},t)$ are the local densities of A and B and D the diffusion constant and R the reaction rate. For a d-dimensional homogeneous system in which at time $t = 0$ there is an equal number of A and B particles randomly distributed, (1) predicts that the densities of both A and B species will decay as $a \simeq b \simeq 1/t$, while numerical simulations lead $a \simeq b \simeq t^{-\frac{d}{4}}$ for $d \leq 4$ [1]. This discrepancy can be explained by studying the rôle played by the fluctuations and it was shown [1] that these fluctuations were relevant below the upper critical dimension $d_{up} = 4$.

We have studied two new situations, both theoretically and by numerical simulations based on a cellular automata model for reaction-diffusion [2].
The first situation considered differs from the one described above by the fact that the initial configurations of A and B particles are random but identical (since only head-on collisions lead to reaction, complete annihilation does not ensue). The lack of long-range fluctuations in the difference in the particle densities leads to the prediction [3] $a \simeq b \simeq t^{-\frac{d}{2}}$ for $d \leq 2$, confirmed by numerical simulations in one, two and three dimensions.

The second situation concerns the case where at time $t = 0$, the two diffusing reagents are separated in space and will react in a confined region called the reaction front. This problem has been studied in the mean-field approximation by Gálfi and Rácz[4]. We have studied the rôle played by the fluctuations from different points of view [2, 5, 3], namely a scaling theory, microscopic arguments about the range of the fluctuations, and numerical simulations in one and two dimensional systems. All these approaches corroborate the fact that the upper critical dimension is in this case $d_{up} = 2$. The reaction front $R(x,t)$ obeys the scaling form

$$R(x,t) =< ab > (x,t) = t^{-\beta}\mathcal{R}(xt^{-\alpha}) \tag{2}$$

In one dimension, one finds important deviations of the exponents α and β from their mean-field values while, for the upper critical dimension $d = 2$, logarithmic corrections to the mean field predictions show up [5].

Generalisation to the reaction $nA + mB \rightarrow C$ are also considered [5, 3].

The most recent numerical simulations reported in this note have been performed on the Connection Machine CM-2a installed at the University of Geneva.

References

[1] D. Toussain and F. Wilczek, J.Chem.Phys. **78**, 2642 (1983)

[2] B. Chopard and M. Droz, Europhys. Lett. **15**, 459, (1991).

[3] S. Cornell, B. Chopard and M. Droz , in preparation.

[4] L. Gálfi and Z. Rácz, Phys.Rev **A38**, 3151 (1988)

[5] S. Cornell, B. Chopard and M. Droz , Phys.Rev. **A**, to appear (1991).

The elastic constants of thin $Si_{1-x}Ge_x$ films determined by Brillouin scattering

M.Mendik, M.Ospelt, H.v.Känel, P.Wachter
Laboratorium für Festkörperphysik, ETHZ, 8093 Zürich

Abstract

Surface acoustic waves (SAW's) on ultrathin (h=80–4000Å) $Si_{1-x}Ge_x$ films grown on Si(100) have been measured by means of Brillouin scattering (BS) both as a function of $\mathbf{k}\cdot h$ and the direction of $\mathbf{k}$ in the sample plane ($\mathbf{k}$ wavevector of the SAW, h thickness of the film). The sampling depth of the SAW's in the GHz range extends to 4000Å. Therefore the velocity of a SAW on thinner films (h<4000 Å) is determined by the elastic properties both of the film and the substrate. The angular dispersion (AD) of SAW's on (100) oriented thin films has been evaluated numerically for different thicknesses and compared with the measurements.

The study of the elastic properties of thin films grown on a substrate is an important task in materials science. Since the development of the (3+3) tandem interferometer by Sandercock [1] BS has become an important tool to determine the elastic properties of thin films. Results were reported for several metallic thin films, multilayers and superlattices [2]. In order to obtain the elastic constants, Rayleigh–and Sezawa modes have been measured both as a function of $\mathbf{k}$ and h. This method deals with several films of different thicknesses and therefore the obtained elastic constants are an average over all considered films. In this work, on contrary, single (cubic) $Si_{1-x}Ge_x$ thin films grown on Si(100) are characterized on measuring the AD of SAW's.

The AD of SAW's has been computed using a continuum mechanical model [3], neglecting crystallographic imperfections and assuming perfect interfaces.The parameters of the model are the elastic constants C_{11},C_{44},C_{12} and the densities of both the substrate and the layer. In contrast to other authors we avoided the ultrasonic data for the substrate and utilized the elastic tensor obtained from the AD of SAW's on bare Si(100) substrate [4].

We used the TM polarized λ=514 nm line of an Ar laser as the excitation source with an incident power of 30–80 mW. The backscattered light was collected by an objective and focused into a (3+3) tandem interferometer. During experiment the samples were in air and at room temperature. For the SAW velocities an error of 1% has been estimated.

All $Si_{1-x}Ge_x$ alloys were grown by MBE on (100) oriented n–type Si wafers [5]. $Si_{.50}Ge_{.50}$ and $Si_{.65}Ge_{.35}$ with h=5000 [6],600,80 Å and h=2400,1170 Å respectively have been investigated.

Fig1) shows the velocity of SAW's as a function of the direction of $\mathbf{k}$ in the sample plane (AD) on various layers with different thicknesses and the two concentrations. For comparison the AD on bare Si(100) is also shown. In addition, no higher order modes (Sezawa) have been observed. The incident angle has been kept fixed at 70o. The full lines have been computed using the following values: C_{11}=161.4, C_{44}=75.9, C_{12}=61.3 GPa, ρ=2.3gr/ccm for the substrate, C_{11}=144, C_{44}=67.3, C_{12}=54.7 GPa, ρ=3.8gr/ccm and

C_{11}=149.5, C_{44}=58.7, C_{12}=48.1 GPa, ρ=5.3gr/ccm for $Si_{.50}Ge_{.50}$ (h=80Å) and $Si_{.65}Ge_{.35}$ respectively. The samples are: ▲: Si, ▼: $Si_{.49}Ge_{.51}$(80Å), ●: $Si_{.54}Ge_{.46}$(600Å), ○: $Si_{.66}Ge_{.34}$(1170Å), △: $Si_{.66}Ge_{.34}$(2400Å), ■: $Si_{.49}Ge_{.51}$(5000Å).

Fig1)

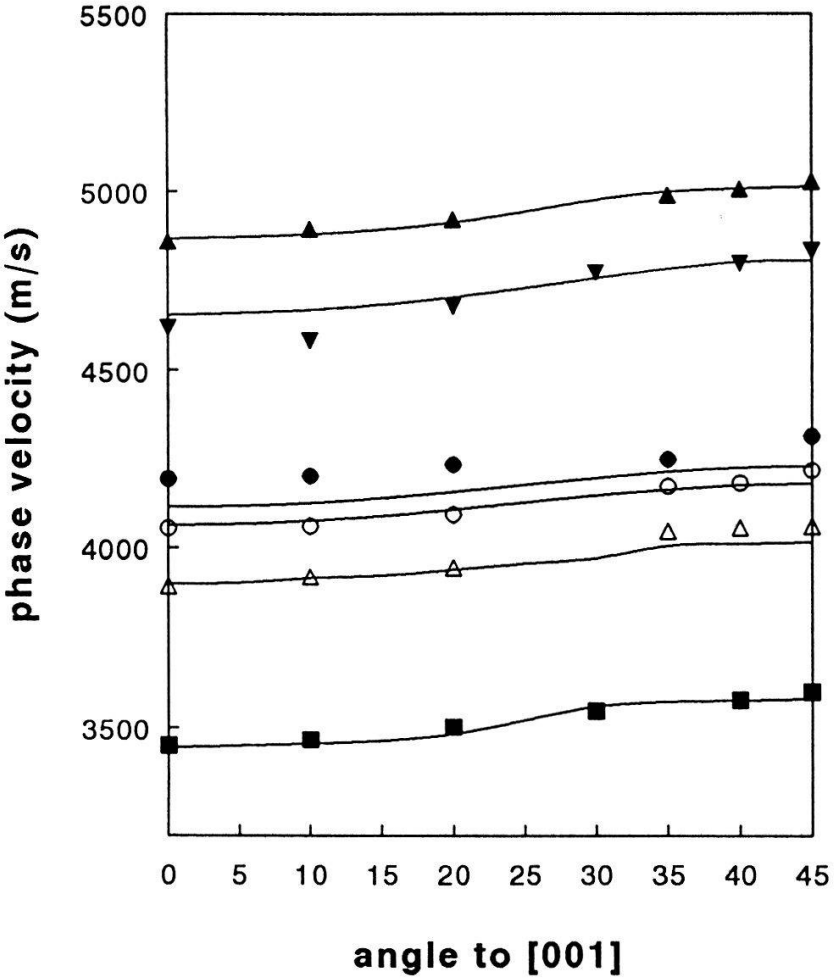

In conclusion, we have compared the measured AD of $Si_{1-x}Ge_x$ with the calculated one using the linearly interpolated elastic constants of the constitutents and found in general good agreement between theory and experiment.

References

[1] J.R.Sandercock,Solid State Commun.26.547(1978).
[2] F.Nizzoli,in "Dynamical Properties of Solids", Vol.6,ed.by G.K.Horton pp. 284–335,(1990).
[3] G.W.Farnell,in "Physical Acoustics",ed.by W.P.Mason, Vol.VI, pp. 109–166, Acad.Press, N.Y.(1970).
[4] M.W.Elmiger,J.Henz,H.v.Känel,M.Ospelt,P.Wachter,Surface and Interface Analysis,14,18(1989).
[5] M.Ospelt,J.Henz,E.Müller,H.von Känel,Mat.Res.Soc.Symp.Proc.Vol.198,1990.
[6] M.Mendik,M.Ospelt,H.von Känel and P.Wachter,Applied Surface Science 50(1991) 303–307.

EXTRACTION OF MOSFET PARAMETERS AT LOW DRAIN BIAS

Y. Haddab, M. A. Py, Z. M. Shi, H.-J. Bühlmann, M. Ilegems
Institute for Micro- and Optoelectronics, EPFL, 1015 Ecublens-Lausanne

Abstract

It is well known that the electron mobility near 300 K in Si-MOSFET's follows a power-law dependence on the inversion layer concentration n_s with a negative exponent k ($-1/3 \leq k \leq -1/6$) in an intermediate range of n_s. We present here a method for the extraction of MOSFET parameters in the low longitudinal field regime based on a simple linear charge-control model and on this power-law dependence.

We have developed an analytical method to extract FET's parameters at low drain bias [1]. It is based on a simple charge-control model which gives a uniform electron concentration in the channel under low drain bias conditions:

$$n_s = C_{eff}\, V_g^*/q\,, \tag{1}$$

C_{eff} being the effective gate capacitance per unit area, q the electronic charge and V_g^* the effective gate voltage, defined as $V_g^* = V_g - V_t - V_{ds}/2$, where V_t is the threshold voltage, V_{ds} the drain to source voltage and where the source and drain series resistances (respectively R_s and R_d) are assumed to be comparable. This analytical method takes into account the power-law dependence of the low-field mobility carrier concentration in the channel [2,3]:

$$\mu = \mu_o\, (n_s/n_{so})^k, \tag{2}$$

which holds in an intermediate range of n_s where phonon scattering dominates [4], n_{so} being the inversion layer concentration at a given gate voltage $V_g^* = V_g^*{}_{,nor}$ here equal to 1 V, μ_o being the mobility for $n_s = n_{so}$. We must have $n_s >> n_{depl}$ to get the power-law dependence [5]. Besides, for high values of n_s, roughness scattering dominates and this power-law does not hold any more [3].
By combining (1) and (2) with the expression of the current at low drain bias, and by deriving the expression for the transconductance g_m, one can obtain [1] (assuming $R_s + R_d$ independent of V_g^*):

$$\frac{I_{ds}}{(V_{ds}\, g_m)^{1/2}} = \sqrt{\frac{\beta'}{1+k}}\ \left(\frac{V_g^*}{V_{g,nor}^*}\right)^{1+\frac{k}{2}} \tag{3}$$

$$\frac{I_{ds}}{g_m V_g^*} - \frac{1}{1+k} = \frac{\beta'}{1+k}\,(R_s + R_d)\ \left(\frac{V_g^*}{V_{g,nor}^*}\right)^{1+k} \tag{4}$$

$$R_{ch} = \frac{V_{ds}}{I_{ds}} - (R_s + R_d) = \frac{1}{\beta'}\left(\frac{V_g^*}{V_{g,nor}^*}\right)^{-(1+k)} \tag{5}$$

where β' is defined as: $\beta' = \frac{W}{L}\mu_o\, C_{eff}\, V_{g,nor}^* = \frac{W}{L}\mu_o\, q\, n_{so}$.

For the actual analysis, we proceed in the following way: the expression on the left-hand side of (3) is constructed and V_t is adjusted to get the best fit of this expression to a power-law of V_g^* (Figure 1). We then get the values of k and β', which allows us to construct the left-hand side expression of (4). A slight adjustment of the k-value might be needed, and $(R_s + R_d)$ is then obtained (Figure 2). Finally, k, β'

and ($R_S + R_d$)-values can be checked by plotting $R_{ch} = R_t - (R_S + R_d)$, the channel resistance, as a function of V_g^*. We have applied this method to a n-channel MOSFET. The results are given in Table I.

TABLE I. Results of the analysis applied to a n-channel MOSFET biased at 50 mV with W/L = 123μm/0.8μm, and a substrate doping $N_A = 2.4 \times 10^{16}$ cm^{-3}. The SiO_2 oxide thickness was about 400 Å ($C_{eff} = 86$ nF/cm^2). The intermediate range of n_s mentioned earlier corresponds to 0.5 V < V_g^* < 5.0 V.

Parameter	V_t (V)	k	β' (mS)	$R_S + R_d$ (Ω)
Eqn (3)	0.30	- 0.19	8.8	
Eqn (4)		- 0.17		9.1
Eqn (5)		- 0.16	8.9	

The parameter-values obtained through the different steps of the analysis are in very good agreement with each other. The obtained k-value, -1/6, is higher than the -1/3 expected when two-dimensional lattice scattering within one subband dominates the mobility [5]. This tends to show that intersubband scattering is important in this device [3].

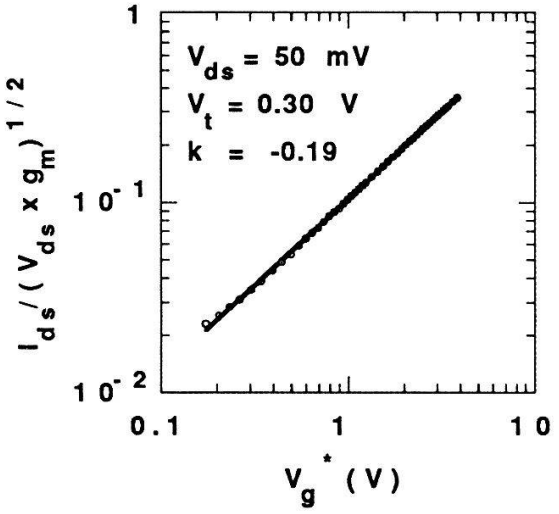

FIG. 1. Plot of the left-hand-side of (3) as a function of V_g^* for the MOSFET defined in Table I. The very good fit with a power-law according to (3) gives the values of the parameters listed in Table I.

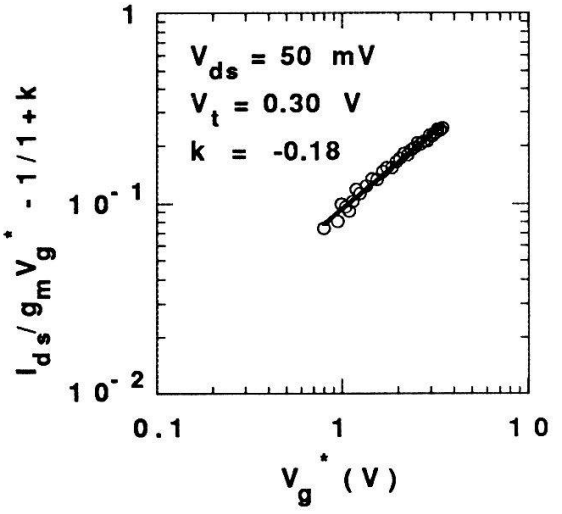

FIG. 2. Plot of the left-hand-side of (4) as a function of V_g^* for the same MOSFET. Since we have g_m in the denominator of the expression, there is more dispersion in the data than in Fig.1 (where we have the square root of g_m in the denominator).

In conclusion, we have developed and tested an original method to extract MOSFET's parameters at low drain bias using a power-law dependence of mobility on carrier concentration. This method can also be applied to other types of FET's, such as MODFET's [1,6].

Acknowledgements

This work has been partially supported by the Swiss National Science Foundation. We would also like to thank the CSEM-Neuchâtel and Dr. M. Dutoit for providing the MOSFET's.

References

[1] M. A. Py et al., to be published.
[2] F. Fang and A. B. Fowler, Phys. Rev, **169**, 619 (1967).
[3] H. Ezawa et al., Japn. J. Appl. Phys., **13**, 126 (1973).
[4] D. S. Jeon and D. E. Burk, IEEE Trans. Elec. Dev., **36** 1456, (1989).
[5] S. Kawaji, J. Phys. Soc. Jap, **27**, 906 (1969).
[6] M. A. Py et al., Microelec. Eng., **15**, 577 (1991).

No Feedback Control of a Kármán Vortex Street

F. Ohle, M. Brede* and H. Eckelmann

Institut für Angewandte Mechanik und Strömungsphysik der Universität,
D-3400 Göttingen, Bunsenstr. 10, Germany
* Max-Planck-Institut für Strömungsforschung, D-3400 Göttingen, Germany

The possibillity to apply a nonlinear no feedback control to a Kármán vortex street of a circular cylinder will be discussed. Emphasis of this paper is to show that a control can be effectivelly achieved only if the vortex street is stimulated at the cylinder.

A method to control the dynamics of an experimental system to a preselected dynamics without feedback was developed recently [1]. Yet, this method was applied experimentally only to a mechanical oscillator [2]. In addition the control was investigated theorectially with the help of the van der Pol oscillator, the Lorenz, and the Roessler system. Good results with the nonlinear no feedback control could be obtained in all these cases (see e.g. Ref.[3]). The no feedback control is based on the following idea:
Assume, that an experimenal system can be described by a differential equation of the form

$$\dot{\vec{x}}(t) = \vec{E}(\vec{x}, t) + \vec{f}(t), \tag{1}$$

where $\vec{f}(t)$ defines the control force. If such an equation is unknown or cannot be solved exactly, a low-dimensional model

$$\dot{\vec{y}}(t) = \vec{M}(\vec{y}, t) \tag{2}$$

has to be determined, which describes accurately the temporal dynamics of the experiment. In addition a desired behavior of the system is specified by the preselect dynamics

$$\dot{\vec{z}}(t) = \vec{G}(\vec{z}, t). \tag{3}$$

Then the appropriate driving force

$$\vec{f}(t) = \vec{G}(\vec{z}, t) - \vec{M}(\vec{z}, t) \tag{4}$$

can be calculated. For $\vec{x}(t) = \vec{z}(t)$ and $\vec{M}(\vec{y}, t) = \vec{E}(\vec{x}, t)$ the experimental system immediately locks into the goal dynamics $\vec{z}(t)$ and the control is accomplished. The most crucial point of this method is, if Eq.(1) is unknown or cannot be solved, that then a model of the system dynamics (Eq.2) is needed. Such a model can be constructed for example from measured time signals [4].

The possibility to apply the above procedure to a vortex street will be discussed in the following. Since in general Eq.(1) is the Navior-Stokes equation, an accurate low-dimensional model has to be determined. In the present case, this was accomplished by extracting from

measured time signals a two-dimensional third order differential equation. The time signals were measured by a hot wire probe place on one side of the vortex street (Fig.1). It was shown elsewhere [4], that this model can reproduce and predict the vortex shedding dynamics accurately

The control was realized by superimposing sound from two loudspeakers placed outside the flow (Fig.1). However, by using this experimental arrangement no effective control was achieved [5]. The question which arises is; "Why does the model predict the response to sinusodial and square wave sound excitation accurately, but fails with the nonlinear no feedback control?" The main reason is that the model was derived from the developed wake and not from the vortex formation at the cylinder. Since the added control force (sound) acts on the cylinder boundary layer, i.e on the vortex seperation, and since the model is derived from the knowledge downstream in the wake, no effective control should be expected. Different to a mechanical oscillator, here every vortex can be considered as a single independent one where no information is transfered from one vortex to an other. Modelling and control should therefore be achieved via the boundary layer at the cylinder. The dynamics of a boundary layer can be expected to be similar to that of a mechanical oscillator, where the rear stagnation-point is the equlibrium position F (Fig.2). A successful control of the vortex seperation from the cylinder can be realized by modelling the pressure fluctuations and than stimulate the seperation by the calculated control force via the pressure field. Experiments are in progress.

References

[1] A. Hübler and E. Lüscher, Naturwissenschaften, **76**, 67, (1989)
[2] R. Georgii, W. Eberl, E. Lüscher and A. Hübler, Helv. Phys. Acta, **62**, 290, (1989)
[3] E.A. Jackson, Beckman Institute, Urbana-Champaign, Ill 61801, Tech. Rep. CCSR-90-8
[4] F. Ohle and H. Eckelmann, submitted to Phys. Fluids A (1991)
[5] E. Roesch, Mitteilungen aus dem MPI für Strömungsforung, Nr. 99, (1991)

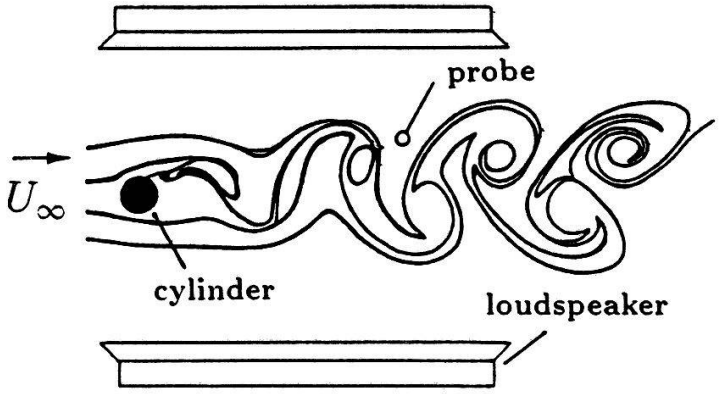

Fig.1: Vortex street with control arrangement used so far

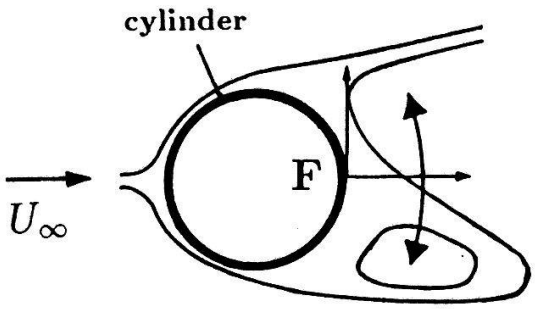

Fig.2: Modelling and control via the pressure fluctuations at the cylinder

Numerical Calculation of Breakdown Channel Formation in Silent Discharges in CO_2

W. Egli and B. Eliasson
ABB Corporate Research Center Switzerland, 5405 Baden-Dättwil, Switzerland

We present two-dimensional, time-dependent calculations of microdischarge formation during electrical breakdown of a silent discharge in a plane-parallel gap. The silent discharge is a high pressure discharge, where one of the electrodes is covered by a dielectric. If one applies a voltage which exceeds the Paschen breakdown voltage to the gap, the electrical breakdown of the gas results in a series of short-lived (ns) microdischarges, which are evenly distributed over the electrode surface [1]. We calculate the formation of one such microdischarge. In an electronegative gas like CO_2 the electrons attach themselves to the CO_2 molecules shortly after they are created and form negative ions. After breakdown there is a conducting channel connecting the electrodes. It is some hundred μm in diameter and it consists mostly of positive and negative ions. In this example we have assumed that the dielectric is on the anode. The electron and ion avalanches deposit charges on the anode, which thus generated an electric field which is directed against the applied field.

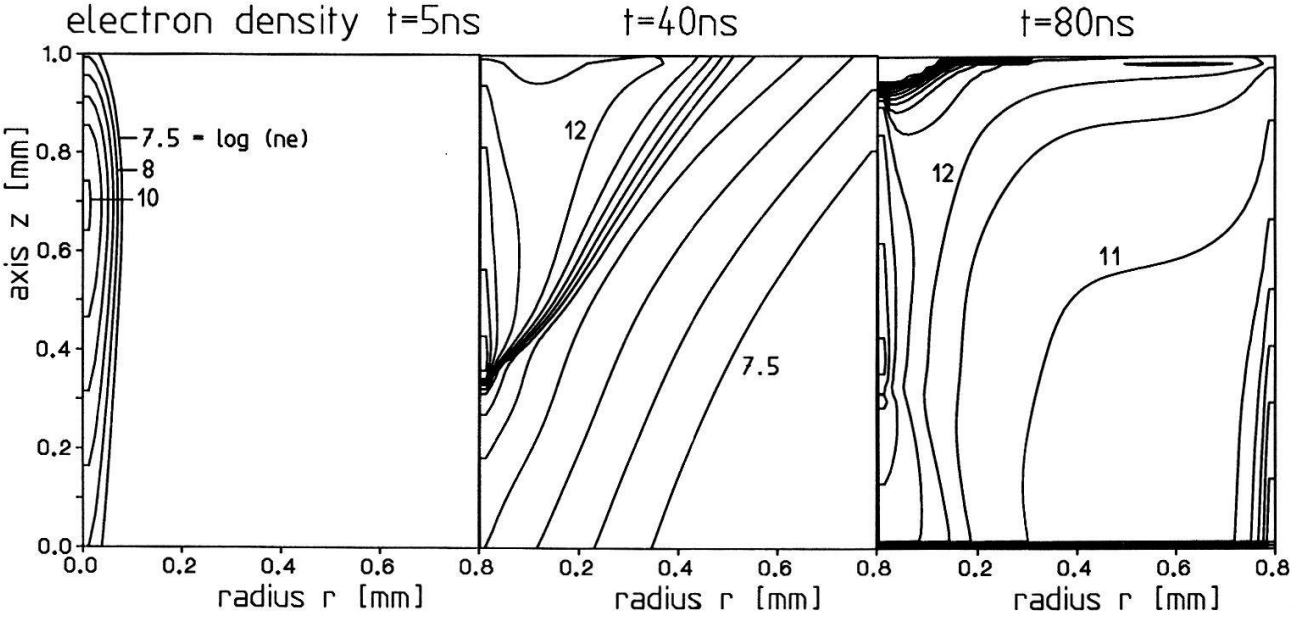

Fig. 1: Electron densities in space at three different times.
(Applied field = 160 Td, gap = 1 mm, dielectric thickness = 0.8 mm, $\varepsilon_r = 3$)

The equations that govern the behaviour of the charged particles in an electric field are the equation of continuity for the electrons (n_e) and the ions (n^+, n^-) and the Poisson equation for the potential Φ or the electric field E. The mathematical formulation of the problem has been given elsewhere ([2],[3]). Here we have, in addition, considered ionic recombination. The boundary conditions for the ions are: n^- (cathode, t) = 0, n^+ (anode, t) = 0. The mobility of the electrons was assumed to be 500 $cm^2/Vsec$ and for the ions 1 $cm^2/Vsec$. The ionization coefficient α was written in the approximation given in [3] by using data taken from [4]. With E/n units of Td = 1.10^{-17} Vcm^2 and α/n in units of 1.10^{-17} cm^2 with n being the total gas density (2.410^{19} cm^{-3} at 1 bar and 300 K) we get:

$$\ln (\alpha/n) = -383 \exp (-0.9654 \ln (E/n)) + 0.2633 + 0.3672 \ln (E/n)$$

For the electron attachment coefficient η we use a polynomial expression. By using the same units as above we get for $(E/n) < 160$ Td:

$$\eta/n = \max [0, 1.25310^{-5}(E/n) - 6.7210^{-6}(E/n)^2 + 2.31610^{-7}(E/n)^3 - 1.2110^{-9}(E/n)^4]$$

For $(E/n) > 160$ Td we put $\eta/n = 0$.

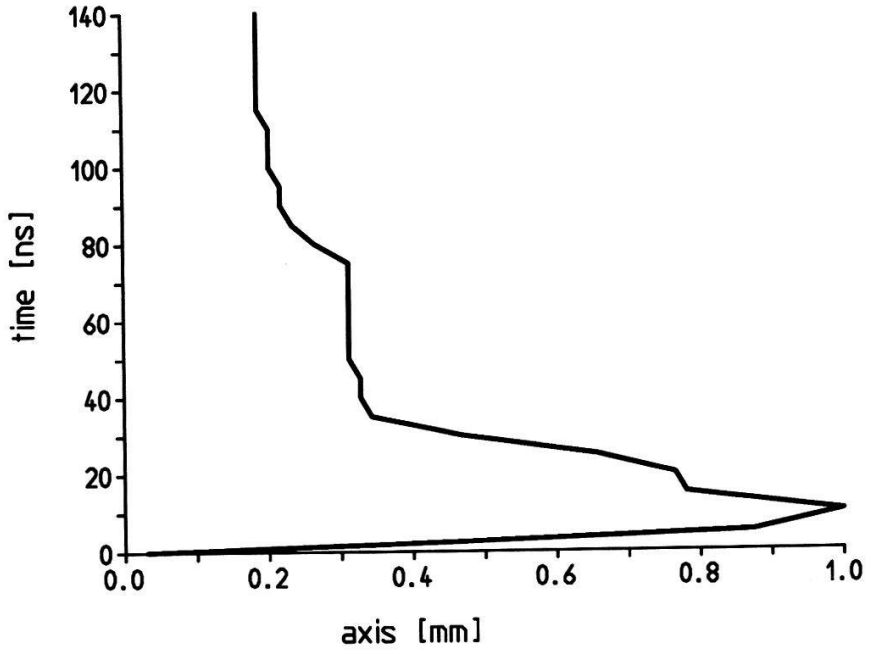

Fig. 2: Location of the electron avalanche front as a function of time. The avalanche is "reflected" at the anode. The front is defined at the 20 % value of max (n_e).

In Fig. 1 we show the distribution of the electron densities in space for three different times. The wave reflected from the anode towards the cathode is evident.

The space charge field of the initial electron avalanche moving towards the anode is reflected at the anode and generates a pseudo-avalanche moving towards the cathode. The electron avalanche propagating towards the cathode is caused by the propagation of this space charge field. These two avalanches propagate at different velocities. In Fig. 2 we show the location of the avalanche front as a function of time. The two different velocities of propagation for the anode and cathode avalanches correspond to the derivatives of the upper and lower traces in Fig. 2. The final velocity for times $t > 40$ nsec corresponds approximately to the ionic drift velocity.

References

[1] B. Eliasson and U. Kogelschatz, IEEE Trans. Plasma Science, 19(2), April 1991, 309-323.

[2] W. Egli and B. Eliasson, Helvetica Physica Acta, 62, 1989, 302-305.

[3] B. Eliasson and W. Egli, ICPIG XIX, Belgrade, July 10-14, 1989.

[4] P. Laboire, J.M. Rocard, J.A. Rees, Electronic Cross Sections - Macroscopic Coefficients, Dunod, Paris, 1971

Hydrogenation of CO_2 in a Silent Discharge

B. Eliasson, F.G. Simon, W. Egli, and P. Brunner*
ABB Corporate Research Center Switzerland, 5405 Baden-Dättwil,
Switzerland and Vilab AG*, 3014 Bern

One of the methods for dealing with increasing greenhouse gas emissions is to separate CO_2 from flue or combustion gases of power plants and convert it to methane or methanol with the aid of pollution free hydrogen. The production of methanol from CO derived from coal or natural gas and steam at high temperatures (200-270°C) and pressures (50-150 bar) is a well known process. What is not so well known is how to make methanol from CO_2 and H_2 at lower temperatures (100-150°C) and preferably lower pressures (1-30 bar). The ultimate goal of this work is to contribute to the development of a thermal catalytic reactor which works in the above range and uses mainly CO_2 as feed gas for C and O atoms.

In the initial stages of this work we have used an experimental reactor to activate CO_2 and H_2. This reactor consists of a silent discharge tube made of quartz with a metallic inner electrode, which can be cooled. On the top of the quartz tube there is a metallic mesh, which is used as a second electrode. The silent discharge consists of a multitude of microdischarges, which last only

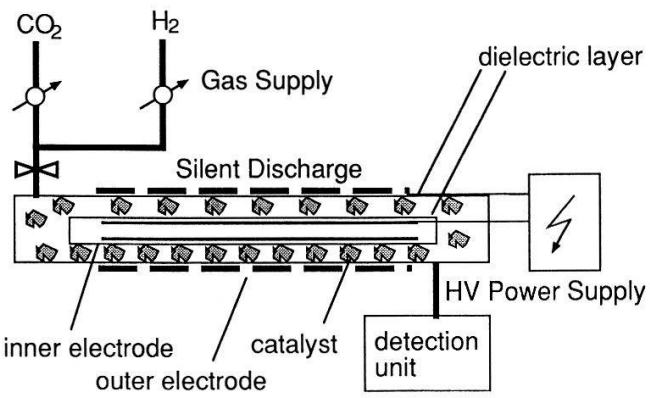

Fig. 1: The experimental set-up

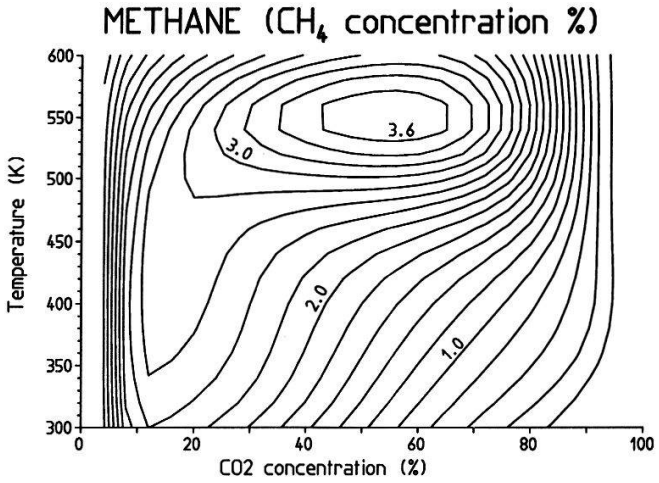

Fig. 2: Calculated yield of methane (1 bar) vs. temperature and CO_2/H_2

few nanoseconds [1]. During this time they generate electrons, which dissociate and excite the molecules and thus initiate chemical reactions which lead to higher hydrocarbons.

We have both used the discharge with and without a catalyst. The catalytic material was deposited on a quartz dielectric and put into the discharge gap. The set-up is shown in Fig.1. We applied high voltage of high frequency (20 kV and 40 kHz) to a gap of 3 mm width at a pressure of 1 bar. Neither the pressure nor the gap width were changed in these initial experiments. Only the residence time was adjusted (360 seconds) to maximize the output of the species generated.

We furthermore established a computer model of the processes taking place in such a discharge. By simulating a number of microdischarges occuring in the discharge gap, and combining these with the chemical activity taking place, we could calculate the species generated both as a function of composition and temperature for a fixed time (Fig.2) as well as their temporal development (Fig.3). The modelling of the microdischarges is based on our experience with modelling of microdischarges for ozone generation and the production of excimers in silent discharges. The chemical reactions used in our model have been taken from Ref. [2]. These reactions have been extended by reactions specifying the dissociative interaction of electrons and molecules, of the kind

$$e + CO_2 \rightarrow CO + O + e$$

We have measured the CO and CH_4 generated as a function of the initial mixture of CO_2 and H_2.

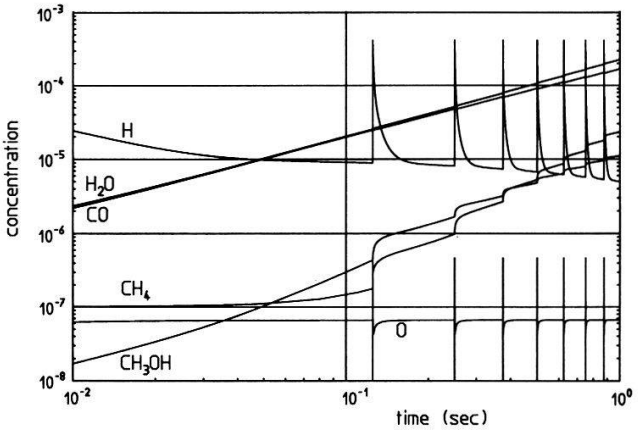

Fig. 3 Temporal development of a series of microdischarges in 20% CO_2 and 80% H2 at 1 bar and 400K. The pulses are 10 msec apart.

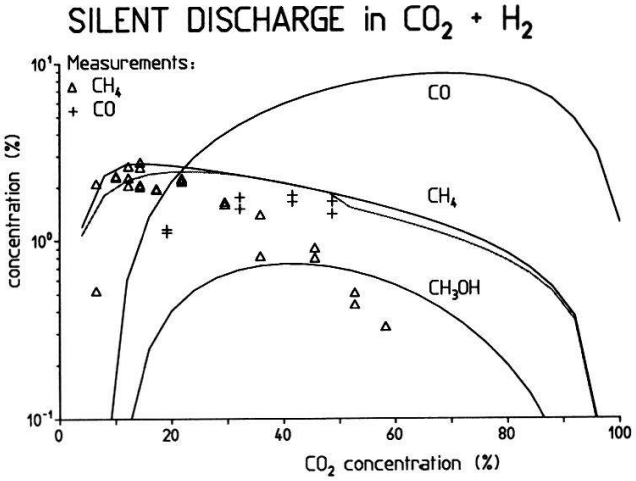

Fig. 4 Measured and calculated concentrations CH_4, CO and CH_3OH as a function of CO_2 and H_2 after a reaction time of 360 sec.

In Fig.4 we have plotted some measurements and compared these to calculations. The result of the computer model are in fairly good agreement with the measured methane values but give a somewhat higher rate for the production of CO. The maximum conversion rate of CO_2 to CH_4 is on the order of 3% without a catalyst. The catalysts used were combinations of CuO/ZnO. The yield increased by 30% by using a CuO catalyst deposited on dielectric quartz wool. Only small amounts of CH_3OH where detected, less than 100 ppm.

It is to be expected, that once the discharge is optimized by adjusting the pressure, the gap width, the temperature and the catalysts used, one could increase the yields markedly.

References

[1] B. Eliasson and U. Kogelschatz, IEEE Trans. Plasma Science, 19(2), April 1991, 309-323.

[2] W. Tsang, J. Phys. Chem. Ref. Data, 16(3), 1987, 471-508.